ACS APPLIED MATERIALS & INTERFACES

Research Article

www.acsami.org

# Interface-Engineered Resistive Switching: $CeO_2$ Nanocubes as High-Performance Memory Cells

Adnan Younis,[†] Dewei Chu,*[,†] Ionsecu Mihail,[‡] and Sean Li[†]

[†]School of Materials Science and Engineering, University of New South Wales, Sydney, 2052 New South Wales, Australia

[‡]Australian Nuclear Science and Technology Organization, New Illawarra Road, Lucas Heights, 2234 New South Wales, Australia

Supporting Information

**ABSTRACT:** We reported a novel and facile approach to fabricate self-assembled $CeO_2$ nanocube-based resistive-switching memory device. The device was found to exhibit excellent bipolar resistive-switching characteristics with a high resistance state (HRS/OFF) to low resistance state (LRS/ON) ratio of $10^4$, better uniformity, and stability up to 480 K. The presence of oxygen vacancies and their role was discussed to explain the resistive-switching phenomenon in the fabricated devices. Further, the effect of the film thickness on carrier concentrations and estimated electric field strength with the switching (OFF/ON) ratio were also discussed.

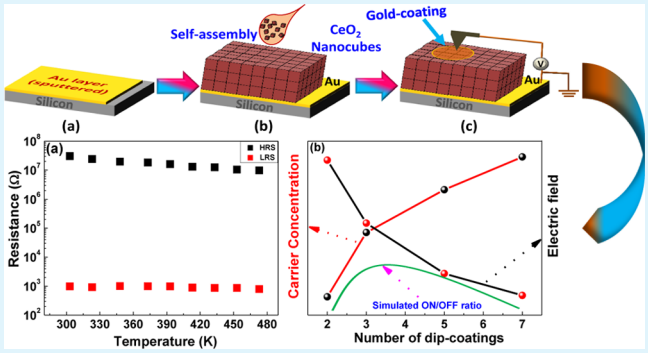


**KEYWORDS:** *hydrothermal process, metal oxide, self-assembly, oxygen vacancies, resistive switching, cerium oxide*

## INTRODUCTION

Recently, resistive random access memories (RRAMs) have been intensively studied as one of the next-generation nonvolatile memory technologies. In comparison with traditional nonvolatile memories (e.g. flash memory), RRAM has unique advantages with much faster writing/reading rate, smaller cell size, lower operating voltages, less power consumption, etc.[1,2] The memory cell of a RRAM is usually built on a capacitor-like metal/metal oxide/metal configuration, where the middle layer (metal oxide) acts as an active layer for a resistive-switching (RS) device. Although RS phenomena have been observed in many oxides , such as ZnO,[3] $TiO_2$,[4] NiO,[5,6] $HfO_2$,[7] and $CeO_2$,[8,9] several challenges still remain unsolved. For example, the miniaturization of a RRAM cell has approached fundamental limits by using conventional fabrication technology in memory industries. Recent advances in the chemical bottom-up method provide an alternative approach to surmounting the obstructions of the limitations.[10,11] However, the OFF/ON ratio for the memory devices fabricated by chemical methodologies is not only very low but also unstable,[4,12] which are associated with the low crystallinity and large defect concentration.

It is believed that oxygen vacancies play an important role in tuning the intergrain interface barrier and stimulating redox processing, thus determining the RS behavior in metal oxides.[12−14] However, too high concentration of oxygen vacancies could decrease the high resistance state (HRS/OFF state) value and thus result in a relatively low OFF/ON ratio. On the other hand, an inhomogeneous distribution of oxygen vacancies within different cells may affect the device stability under stress and high temperatures. Therefore, the fabrication of a pseudoperfect structure with controllable oxygen vacancies in its concentration and distribution is highly desirable. Owing to the unique morphology of the individual entity, the nanocubes can be ideal candidates that can artificially be arranged into a highly coordinated square array and then layer-by-layer laid into a three-dimensional system for high-density information storage.

Cerium oxide ($CeO_2$) has some distinctive physical properties such as a high refractive index, a high dc dielectric constant (~26), a small lattice mismatch with silicon (mismatch factor is ~0.35%), etc. These features bring suitability for this material in microelectronic and optic devices.[15−17] On the other hand, the coexistence and reversible valence state transition of $Ce^{3+}$ and $Ce^{4+}$ ions leads to the rapid formation and annihilation of oxygen vacancies that are critical to determining the RS properties. To date, there are limited reports on the fabrication of $CeO_2$ nanostructures for RS devices. Among those studies, the roles of the oxygen vacancies and filamentary process were addressed to explain switching characteristics. In previous studies, for the generation/creation of oxygen vacancies in $CeO_2$ films, different approaches such as the introduction of a $CeO_x$/silicon (Si) interface[18] and utilization of reactive metal electrodes[19] were adopted. The RS characteristics of polycrystalline $CeO_2$ films[12,20] were also studied but with the demerits of a high formation voltage[20] and a low memory window margin.[12] So, the greater challenge in this regard is the

Received: May 26, 2013
Accepted: September 12, 2013
Published: September 12, 2013

   dx.doi.org/10.1021/am403243g | ACS Appl. Mater. Interfaces 2013, 5, 9429−9434

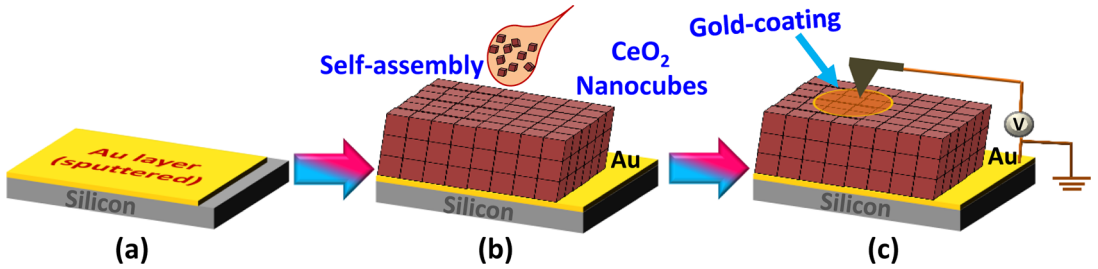


**Figure 1.** (a and b) Schematic diagram for the self-assembly of $CeO_2$ nanocubes to form a RS device (c) setup for $I-V$ measurements.

fabrication of oxygen-vacancy-rich nanostructures that would also be capable of demonstrating excellent RS characteristics.

In the present work, a novel concept of interface engineering in self-assembled $CeO_2$ nanocubes is proposed to fabricate a RRAM device with tunable oxygen-vacancy concentration. It has been found that the devices assembled with $CeO_2$ nanocubes have competitive advantages over current $CeO_2$ thin-film devices.[12] First, the distinct geometry of nanocubes would lead to an excellent RS behavior with a narrow dispersion in the OFF/ON ratio due to the formation of straight and extensible conducting filaments along each nanocube. Second, because of the sub-5-nm size, there are large numbers of interfaces (intergrain regions) among nanocubes, which serve as barriers to increase the total resistance of the memory device in the OFF state (HRS). So, a high value of HRS can effectively increase the overall device OFF/ON ratio. Finally, because of a high oxygen-vacancy concentration, the probability of local oxygen-vacancy migration with a small applied external electric field is high; hence, less electrically induced stress (low set voltage) is required to trigger the RS process. The present device may also facilitate production of an artificial superlattice in the near-perfect structure to disparage interface (grain boundary) scattering of the charge carriers, thus enhancing the conduction probability.

## EXPERIMENTAL SECTION

All chemicals were purchased from Sigma without further purification. $CeO_2$ nanocubes were prepared by using a solvothermal process.[21,22] In a typical synthesis, 15 mL of a 16.7 mmol/L cerium(III) nitrate aqueous solution was added into a 50 mL autoclave, and then a 15 mL mixed solution of toluene and oleic acid (OLA; 0.56 mL, OLA/Ce 8:1) was added. Subsequently, *tert*-butylamine (0.15 mL) was added into the autoclave in an ambient atmosphere. The sealed autoclave was heated at 200 °C for 30 h and then cooled to room temperature. The upper organic crude solution was centrifuged to separate the $CeO_2$ nanocrystals. The separated $CeO_2$ nanocrystals were redispersed into 3 mL of toluene. Afterward, the suspension solution was dip-coated three times to get a self-assembled $CeO_2$ nanocube-based film. The film was treated with ultraviolet radiation for 1 h after every dip-coating to eliminate all organics/extra OLA. The film was finally thermally annealed at 200 °C for 2 h under vacuum. A small area of the electrode (gold, Au) with round patterning and size of about 250 $\mu$m diameter was sputtered through a shadow mask to complete the device fabrication process. The procedure of the self-assembled nanocube structure is summarized in the schematic illustration in Figure 1.

Structural analysis of the as-synthesized $CeO_2$ film was carried out using an X-ray diffractometer with Cu K$\alpha$ radiation. Transmission electron microscopy (TEM) was employed to study the microstructures of the as-prepared materials. For film thickness measurement, the film was coated with Au using a sputter coater to make the film really conductive. Then the film was analyzed with a focused ion beam along with TEM to measure the actual film cross section. X-ray photoelectron spectroscopy (XPS; ESCALAB 250Xi spectrometer) was used to determine the valence states of the cerium ions. The RS characteristics were measured using an Autolab 302N electrochemical workstation controlled with *Nova* software. The varied temperature experiments were performed in the temperature range of 290–480 K, while all of the other electrical measurements were performed in air at room temperature.

## RESULTS AND DISCUSSION

The X-ray diffraction (XRD) pattern shown in Figure 2a demonstrated that all diffracted peaks can be indexed as the

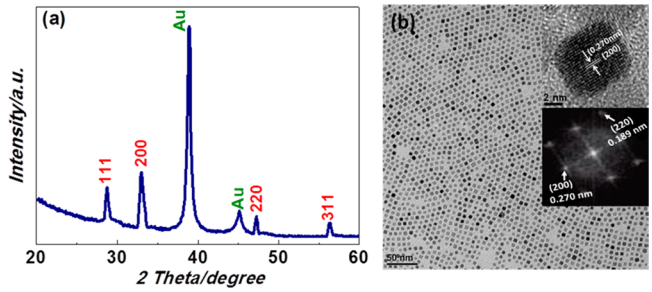


**Figure 2.** (a) XRD pattern of the single-crystalline-like $CeO_2$ nanocubes. (b) TEM image of self-assembled $CeO_2$ nanocubes. Inset: HRTEM and selected-area electron diffraction of a single cube.

face-centered-cubic pure phase [space group $Fm\bar{3}m$ (No. 225)] of ceria (JCPDS 00-034-0394) with excellent crystallinity, and no impurity was detected.

The TEM image of the $CeO_2$ nanocrystals (Figure 2b) exhibits well-dispersed $CeO_2$ nanocubes forming a monolayer of the self-assembly structure on a copper grid. The single-crystalline nature of an individual $CeO_2$ nanocube was verified by a high-resolution TEM (HRTEM) image (inset in Figure 2b). The lattice spacing parallel to facets was 0.270 nm, corresponding to the (100) planes of $CeO_2$, suggesting that the as-prepared $CeO_2$ nanocubes are exposed with (100) facets.

The thickness of the $CeO_2$ nanocube film deposited on a Au-coated Si substrate is around 162 nm (as shown in Supporting Information Figure S1).

Figure 3a demonstrates the size distribution of the as-synthesized $CeO_2$ nanocubes. The typical current–voltage ($I-V$) relationship of the self-assembled $CeO_2$ nanocube-based device is plotted in Figure 3b. A bipolar reversible RS can be visualized, and the device can be set from HRS/OFF to the low resistance state (LRS/ON) at 2.25 V and reset back to its parent state (from LRS to HRS) at −2.56 V.

Theoretically, the memory window can be defined by the two resistance states

$$(R_{OFF} - R_{ON})/R_{ON} \qquad \text{where } R_{OFF} \gg R_{ON}, \text{ and hence}$$

$$\sim R_{OFF}/R_{ON}$$

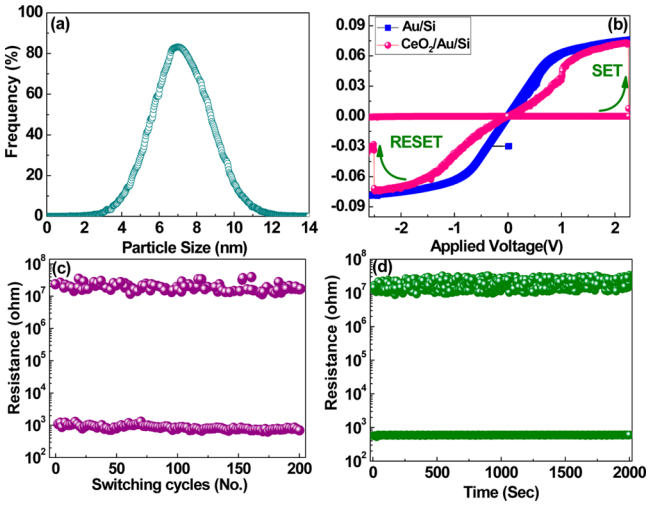


**Figure 3.** (a) Particle-size distributions of the $CeO_2$ nanocubes. (b) $I-V$ measurements on the linear scale. (c) Endurance performance of the device for 200 switching cycles. (d) Data retention performance of the device for 2000 s.

In our case, the window of the as-fabricated device is found to be larger than $10^4$, which is comparable to the best materials fabricated by thin-film technology.[23,24] Such a large margin allows the perimeter of the device circuit to easily distinguish the information stored in the ON and OFF states (Figure 3c). Moreover, this device exhibits reversible and reproducible RS behavior, with high uniformity of the set and reset voltages ($V_{set}$ and $V_{reset}$) and high/low resistances during 30 successive cycles (the $I-V$ curves are illustrated in Supporting Information Figure S2). The resistance states presented in Figure 3c were switched by applying voltage pulses (2.2 V/0.2 ms for the write/ON state and −2.5 V/0.2 ms for the erase/OFF state. Subsequently, the data retention test was carried out in both the OFF and ON states for 2000 s at room temperature, and the result is plotted in Figure 3d.

This demonstrates that the device possesses excellent stability with minimal deviation in OFF/ON resistances under stress, which is desirable for RRAM applications. In general, the lower oxygen-vacancy formation energy [Fermi energies ($E_F$) ranged from 0 to 1.9 eV in $CeO_2$[25]] on/underneath surface results in a higher concentration of oxygen vacancy locally.[26]

Also, for $CeO_2$ nanocrystals, enthalpies (formation energy of oxygen vacancies) of 2.28[27] and 1.84 eV[28] were reported, much lower than 4.2 eV for bulk $CeO_2$.[29] In our case, we also believe that, for a $CeO_2$ nanocube-based thin film, the concentration of oxygen vacancies at/near the surface would be high compared to their counterpart of bulk.

To explain the RS behavior, we proposed a model comprised of oxygen vacancies and their distribution within the device, as shown in Figure 4. Initially, the device is in the OFF state (HRS), and its overall resistance is mainly from the inner region (bulk) of each nanocube, which has extra trapped oxygen ions ($O^{2-}$) and has comparatively high resistance compared to the near-surface region.

Also, large numbers of barriers (interfaces among each nanocube) may have some contribution to enhance the overall device OFF state resistance (~up to $10^7$ Ω). For a positive voltage sweep, the $O^{2-}$ ions (nonbonded) are attracted toward the anode and their migration may create some oxygen vacancies ($V_O$). During this migration, the $O^{2-}$ ions can be trapped in the Au/$CeO_2$ interface, which act as $O^{2-}$ reservoir.[3] However, the $O^{2-}$ ions in the Au gate/$CeO_2$ interface cannot penetrate into the Au gate electrode as interstitial defects or form oxide with this noble metal, and thus they remain trapped at the interface.

When the density of oxygen vacancies ($V_O$) approaches a critical value, a soft-breakdown phenomenon occurs and some percolation paths/conducting filaments are formed between two electrodes. As a result, the electron potential barrier is narrowed down, allowing electrons to tunnel through the potential barrier, and thus a transition from HRS to LRS is observed, as demonstrated in Figure 4b. As supporting evidence, the $I-V$ relationship during this transition state was replotted and found to follow a Fowler–Nodheim tunneling conduction [$\ln(I/v^2) \propto V^{-1}$] process (as illustrated in Supporting Information Figure S3).

On the other hand, for a negative voltage sweep, the $O^{2-}$ ions trapped at the metal/oxide (Au/$CeO_2$) interfaces push toward the cathode (substrate) direction, which immediately triggers the oxygen-vacancy ($V_O$) annihilation process in $CeO_2$ layers. When there are enough $V_O$ annihilation events to block

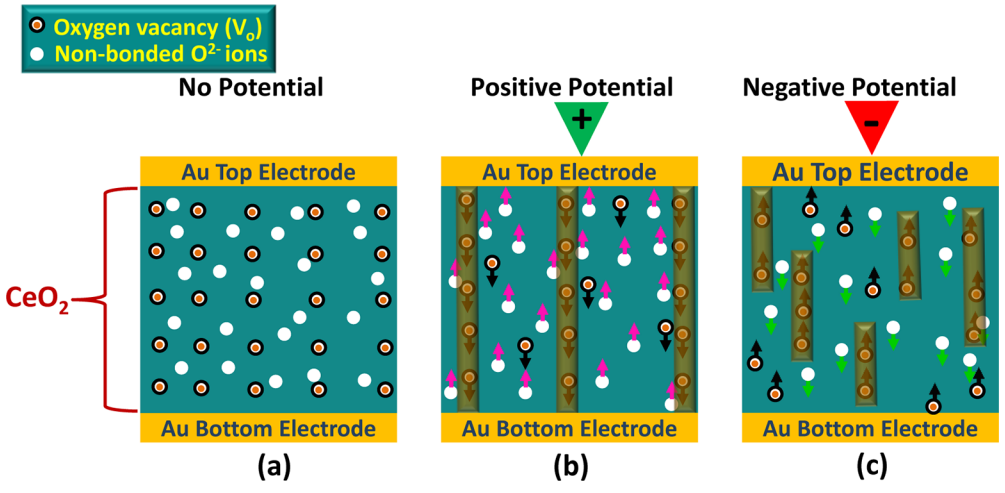


**Figure 4.** Schematic model demonstrating the conduction process in the device (a) without potential, (b) with positive potential, and (c) with negative potential.


dx.doi.org/10.1021/am403243g | ACS Appl. Mater. Interfaces 2013, 5, 9429–9434

the percolation paths or to "switch them off", the device resets itself to HRS again (Figure 4c).

In our previous report,[12] we demonstrated that oxygen vacancies are the dominant character in the RS behavior for $CeO_2$ polycrystalline thin films. It is also worthwhile to mention here that, with decreasing particle size, there are usually many more interfaces in nanocrystalline solids. The energetics for defect formation may be substantially reduced in nanocrystalline oxides, leading to markedly increased levels of nonstoichiometry (oxygen vacancies) and electronic carrier generation.[30] Compared to our previous report[12] ($CeO_2$ thin film with large and irregular grains), the present device ($CeO_2$-based nanocubes), because of reduced grain size, possesses more oxygen vacancies and thus can reflect improved performances such as a high OFF/ON ratio, low device set voltage, and sustainable resistance states at elevated temperatures. Moreover, assuming each single cube as a single resistance unit (resistor), their side-by-side formation (self-assembly) can also form a series resistor circuit. Also, there may be some extra contribution in the overall resistance of the circuit from interfaces among each nanocube. The overall accumulated device resistance (contribution from all tiny resistance units) thus demonstrates a much higher value of HRS ($\sim 10^7$ Ω in the present device) compared to a bulk $CeO_2$ thin film ($<10^3$ Ω)[12] and, therefore, exhibits a high OFF/ON ratio ($>10^4$).

There are several reports that demonstrated that the preferred paths/sites to form a percolation path for the RS process are along the grain boundaries. Recently, in different reports, Lanza et al.[31,32] claimed that the switchable filaments are found to be formed at the dielectric sites where the forming voltages were sufficiently small and also have a high density of oxygen vacancies, which, in the case of the stoichiometric $HfO_2$, was observed exclusively at the grain boundary region. In our case, the regular-shaped crystals (cubic), having more oxygen vacancies at the surfaces compared to their counterparts, reduce the device set voltage and rearrange themselves to form patterned and well-aligned percolation paths, which were lacking in the case of the bulk thin film.[12]

Parts a–d of Figure 5 show (1) the distributions of HRSs and LRSs (measured at 0.5 V) and (2) the set voltage and reset power for the $CeO_2$ nanocube-based device. To drag the statistical data from the present device, 30 consecutive cycles were implemented with the sample.

We further studied the temperature ($T$)-dependent resistance ($R$) of the devices at both the OFF and ON states for the temperature range from room temperature to 480 K (Figure 6a). It can be observed that the resistances at HRS and LRS decrease with increasing temperature, implying semiconductor behavior rather than a metallic one. Furthermore, in the inset of the same figure, the thermal activation energy ($\phi$) was extracted to be 1.03 eV via an Arrhenius plot using the relationship $R = R_0 \exp(\phi_t/kT)$ (where $k$ is the Boltzmann constant), which matches well with the thermal activation energy of 0.8 eV for $CeO_2$.[33]

In order to further investigate the role of oxygen vacancies in switching characteristics, three devices having different thicknesses [by controlling the number of dip coatings (2, 5, and 7 times)] were prepared and their RS performances were evaluated. The film thickness for 7-layer dip coating was found to be ~323 nm (shown in Supporting Information Figure S4), which is almost double that of the film with 3-layer dip coating (Supporting Information Figure S1). The $I$–$V$ measurements

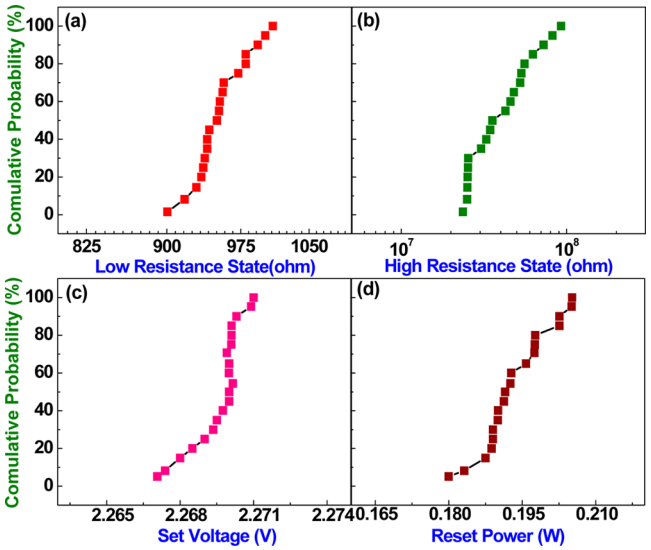


**Figure 5.** Statistical distributions of (a) LRS, (b) HRS, (c) set voltage, and (d) reset power for 30 cycles demonstrating device uniformity.

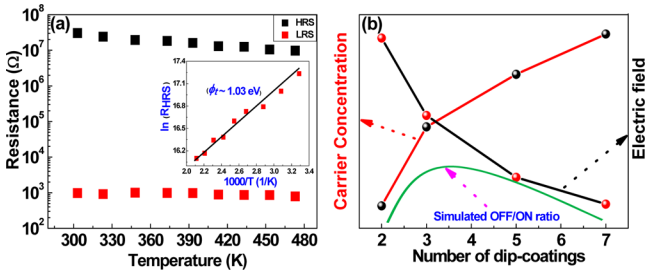


**Figure 6.** (a) Temperature dependence of $R_{OFF}$ and $R_{ON}$ of the device, implying a semiconducting character. The inset is the Arrhenius plot for the OFF state. (b) Variation of the carrier concentration, electric field, and simulated OFF/ON ratios with varying film thickness.

with endurance performances of all devices are shown in Supporting Information Figures S5 and S6. Although all devices showed RS characteristics, the performances of these samples were not as good as expected and their HRS/LRS (OFF/ON) ratio was found to be less than $10^3$. This may be due to a decrease in the effective electric field ($E \sim V/d$) with an increase in the film thickness, thus resulting in a low generation rate of the redox reaction, which is essential for the formation of conducting filamentary paths between the anode and cathode to achieve a high OFF/ON ratio.

For the film with two dip coatings, the oxygen-vacancy concentration may not be sufficient enough to create such a high memory margin up to $10^4$.

Hall effect measurements were carried out to estimate the carrier concentrations in all films, which are also critical for the RS characteristics of the device. Variation in the carrier concentration (with different thicknesses) and estimated electric field strength with different dip coatings are shown in Figure 6b. The optimal carrier concentration and electric field strength were found for the device with 3-layer dip coatings to be well fitted with the simulated OFF/ON ratios (the experimental results are shown in Supporting Information Figure S7).

To further strengthen this argument, we prepared two more samples with 6- and 8-layer dip coatings and did the same test with increased applied potential. Interestingly, the set voltage to

trigger the RS effect in the samples was also found to increase systematically (from 2.6, 2.8, 3.4, and 3.9 V) with increasing film thickness. Instead, the ON/OFF ratios for these samples were decreased from ~$8 \times 10^2$ (5-layer dip coatings) to ~$1.5 \times 10^1$ (8-layer dip coatings).

Therefore, for the formation process, a certain electrical field should be set up to make a conducting path within two electrodes.

Hence, the set voltage becomes higher for thicker films to set up the desired electric field, as shown in Supporting Information Figure S8. Also, the conductivity of HRS was found to increase with increasing film thickness; this may be due to an increase in the carrier concentration with the film thickness. These results are also consistent with our Hall effect measurements, which further verify the increase in the carrier concentration with the film thickness; hence, comparatively high conductance was observed in HRS for thicker films, which causes low OFF/ON ratios.

Finally, the effect of the Au top electrode was also studied. We prepared several devices without the Au top electrode, and their RS characteristics were measured. Surprisingly, all devices exhibit behavior (as shown in Supporting Information Figure S9) similar to that of the Au-coated devices. Therefore, the Au top electrode did not seem to play any significant role in the device RS performance. In order to avoid the RS due to the Au-coated Si bottom electrode, we also used a bare Au−Si substrate without any dip coating, and a short circuit was clearly observed [shown in Figure 3b (blue curve)]. Hence, the possibility of any observable leakages or short currents can be ruled out.

## CONCLUSION

In summary, a self-assembled $CeO_2$ nanocube-based RRAM device was fabricated, and it shows RS characteristics superior to those of conventional RRAM devices from chemical approaches. An OFF/ON ratio higher than $10^4$, an endurance performance of more than $10^2$ cycles, a retention time longer than $10^3$ s, and high uniformity in different switching parameters were achieved. Moreover, the device also reflects the high stability for both resistance states at higher temperatures. A conducting filament model based on oxygen vacancies and their distribution was proposed to explain RS phenomenon in these devices. The optimum level of the oxygen-vacancy concentration for a 3-layer dip-coating device (thickness ~ 162 nm) was further strengthened by exploring variation in the carrier concentrations and estimated electric field strength and examining the OFF/ON ratio with the film thickness. The refinement of the device structure for a further improvement of the device endurance performance and response time with speed is in progress.

## ASSOCIATED CONTENT

### Supporting Information

Cross-sectional TEM image of a $CeO_2$ nanocube-based film, $I-V$ curves of the device for 30 consecutive cycles, curve fitting for Fowler−Nodheim tunneling conduction, $I-V$ curves and endurance measurements for two, five, and seven layers of dip-coating, HRS-to-LRS ratio versus number of dip coatings in the linear scale, $I-V$ measurement with $R-V$ curves for the device without a gold top electrode, and XPS spectra of the Ce 3d region for $CeO_2$ nanocube devices. This material is available free of charge via the Internet at http://pubs.acs.org.

## AUTHOR INFORMATION

### Corresponding Author

*E-mail: D.Chu@unsw.edu.au. Tel.: +61 (0)2 9385 9934. Fax: +61 (0)2 9385 6565.

### Notes

The authors declare no competing financial interest.

## ACKNOWLEDGMENTS

The authors acknowledge financial support from Australian Research Council Project DP110102391 and AINSE Project ALNGRA13533.

## REFERENCES

(1) Szot, K.; Speier, W.; Bihlmayer, G.; Waser, R. *Nat. Mater.* **2006**, *5*, 312−320.
(2) Waser, R.; Dittmann, R.; Staikov, G.; Szot, K. *Adv. Mater.* **2009**, *21*, 2632−2663.
(3) Gao, B.; Yu, S.; Xu, N.; Liu, L. F.; Sun, B.; Liu, X. Y.; Han, R. Q.; Kang, J. F.; Yu, B.; Wang, Y. Y. Electron Devices Meeting, IEDM 2008; IEEE International: Bangalore, India, 2008; pp 1−4.
(4) Chu, D.; Younis, A.; Li, S. *J. Phys. D: Appl. Phys.* **2012**, *45*, 355306−355309.
(5) Nishi, Y.; Jameson, J. R. *Rec. Prog. Resistance Change Memory, Device Res. Conf.* **2008**, 271−274.
(6) Son, J. Y.; Shin, Y. H. *Appl. Phys. Lett.* **2008**, *92*, 222106−222108.
(7) Fang, Z.; Yu, H.; Liu, W.; Wang, Z.; Tran, X.; Gao, B.; Kang, J. *IEEE Electron Device Lett.* **2010**, *31*, 476−478.
(8) Lin, C. Y.; Lee, D. Y.; Wang, S. Y.; Lin, C. C.; Tseng, T. Y. *Surf. Coat. Technol.* **2008**, *203*, 480−483.
(9) Yang, S. M.; Chien, C. H.; Huang, J. J.; Lei, T. F.; Tsai, M. J.; Lee, L. S. *Appl. Phys. Lett.* **2007**, *91*, 262104−262106.
(10) Chu, D.; Masuda, Y.; Ohji, T.; Kato, K. *Langmuir* **2010**, *26*, 14814−14820.
(11) Chu, D.; Masuda, Y.; Ohji, T.; Kato, K. *J. Am. Ceram. Soc.* **2010**, *93*, 887−893.
(12) Younis, A.; Chu, D.; Li, S. *J. Phys. D: Appl. Phys.* **2012**, *45*, 355101−355106.
(13) Younis, A.; Chu, D.; Li, S. *Nanoscale Res. Lett.* **2013**, *8*, 154−159.
(14) Younis, A.; Chu, D.; Lin, X.; Lee, J.; Li, S. *Nanoscale Res. Lett.* **2013**, *8*, 36−40.
(15) Tye, L.; El-Masry, N. A.; Chikyow, T.; McLarty, P.; Bedair, S. M. *Appl. Phys. Lett.* **1994**, *65*, 3081−3083.
(16) Skorodumova, N. V.; Ahuja, R.; Simak, S. I.; Abrikosov, I. A.; Johansson, B.; Lundqvist, B. I. *Phys. Rev. B* **2001**, *64*, 115108−115116.
(17) Copetti, C. A.; Soltner, H.; Schubert, J.; Zander, W.; Hollricher, O.; Buchal, C.; Schulz, H.; Tellmann, N.; Klein, N. *Appl. Phys. Lett.* **1993**, *63*, 1429−1431.
(18) Dou, C.; Kakushima, K.; Ahmet, P.; Tsutsui, K.; Nishiyama, A.; Sugii, N.; Natori, K.; Hattori, T.; Iwai, H. *Microelectron. Reliab.* **2012**, *52*, 688−691.
(19) Liao, Z.; Gao, P.; Meng, Y.; Fu, W.; Bai, X.; Zhao, H.; Chen, D. *Solid State Electron.* **2012**, *72*, 4−7.
(20) Lin, C. Y.; Lee, D. Y.; Wang, S. Y.; Lin, C. C.; Tseng, T. Y. *Surf. Coat. Technol.* **2008**, *203*, 480−483.
(21) Dang, F.; Kato, K.; Imai, H.; Wada, S.; Haneda, H.; Kuwabara, M. *Cryst. Growth Des.* **2011**, *11*, 4129−4134.
(22) Younis, A.; Chu, D.; Lin, X.; Yi, J.; Dang, F.; Li, S. *ACS Appl. Mater. Interfaces* **2013**, *5*, 2249−2254.
(23) Hsu, C. W.; Chou, L. J. *Nano Lett.* **2012**, *12*, 4247−4253.
(24) Jeong, H. Y.; Kim, J. Y.; Kim, J. W.; Hwang, J. O.; Kim, J. E.; Lee, J. Y.; Yoon, T. H.; Cho, B. J.; Kim, S. O.; Ruoff, R. S.; Choi, S. Y. *Nano Lett.* **2010**, *10*, 4381−4386.
(25) Jiang, Y.; Adams, J. B.; Schilfgaarde, V. M.; Sharma, R.; Crozier, P. A. *Appl. Phys. Lett.* **2005**, *87*, 141917−141919.
(26) Tschöpe, A. *J. Electroceram.* **2005**, *14*, 5−23.
(27) Chiang, Y. M.; Lavik, E. B.; Kosacki, I.; Tuller, H. L.; Ying, J. Y. *J. Electroceram.* **1997**, *1*, 7−14.

(28) Hwang, J. H.; Mason, T. O. *Z. Phys. Chem., Int. J. Res. Phys. Chem. Chem. Phys.* **1998**, *207*, 21−38.
(29) Anderson, G. R.; Nowick, S. A. *J. Electrochem. Soc.* **1975**, *122*, 255−259.
(30) Sun, C.; Liab, H.; Chenab, L. *Energy Environ. Sci.* **2012**, *5*, 8475−8505.
(31) Lanza, M.; Bersuker, G.; Porti, M.; Miranda, E.; Nafria, M.; Aymerich, X. *Appl. Phys. Lett.* **2012**, *101*, 193502−193505.
(32) Lanza, M.; Zhang, K.; Porti, M.; Nafria, M.; Shen, Z. Y.; Liu, L. F.; Kang, J. F.; Gilmer, D.; Bersuker, G. *Appl. Phys. Lett.* **2012**, *100*, 123508−123511.
(33) Liang, H.; Raitano, J. M.; He, G.; Akey, A. J.; Herman, I. P.; Zhang, L.; Chan, S. W. *J. Mater. Sci.* **2012**, *47*, 299−307.